

Methods and techniques



Cite this article: Gorilak P, Pružincová M, Vachova H, Olšinová M, Schmidt Cernohorska M, Varga V. 2021 Expansion microscopy facilitates quantitative super-resolution studies of cytoskeletal structures in kinetoplastid parasites. *Open Biol.* **11**: 210131. <https://doi.org/10.1098/rsob.210131>

Received: 14 May 2021

Accepted: 29 July 2021

Subject Area:

microbiology/cellular biology

Keywords:

Trypanosoma brucei, *Leishmania major*, expansion microscopy, microtubule-based cytoskeleton

Author for correspondence:

Vladimir Varga

e-mail: varga@img.cas.cz

†Present address: Max Perutz Labs, University of Vienna, Vienna Biocenter (VBC), Dr Bohr-Gasse 9, 1030 Vienna, Austria.

Electronic supplementary material is available online at <https://doi.org/10.6084/m9.figshare.c.5574313>.

Expansion microscopy facilitates quantitative super-resolution studies of cytoskeletal structures in kinetoplastid parasites

Peter Gorilak^{1,3}, Martina Pružincová¹, Hana Vachova¹, Marie Olšinová⁴, Marketa Schmidt Cernohorska^{2,†} and Vladimir Varga¹

¹Laboratory of Cell Motility, and ²Laboratory of Adaptive Immunity, Institute of Molecular Genetics of the Czech Academy of Sciences, Vídeňská 1083, Prague, 14220, Czech Republic

³Charles University, Faculty of Science, Albertov 6, Prague, 128 00, Czech Republic

⁴IMCF at BIOCEV, Faculty of Science, Charles University, Průmyslová 595, 252 50 Vestec, Czech Republic

PG, 0000-0002-5119-7144; MP, 0000-0002-7146-991X; HV, 0000-0003-0405-5693; MO, 0000-0002-2788-7188; MSC, 0000-0001-9053-8928; VV, 0000-0002-0384-1281

Expansion microscopy (ExM) has become a powerful super-resolution method in cell biology. It is a simple, yet robust approach, which does not require any instrumentation or reagents beyond those present in a standard microscopy facility. In this study, we used kinetoplastid parasites *Trypanosoma brucei* and *Leishmania major*, which possess a complex, yet well-defined microtubule-based cytoskeleton, to demonstrate that this method recapitulates faithfully morphology of structures as previously revealed by a combination of sophisticated electron microscopy (EM) approaches. Importantly, we also show that due to the rapidness of image acquisition and three-dimensional reconstruction of cellular volumes ExM is capable of complementing EM approaches by providing more quantitative data. This is demonstrated on examples of less well-appreciated microtubule structures, such as the neck microtubule of *T. brucei* or the pocket, cytosolic and multivesicular tubule-associated microtubules of *L. major*. We further demonstrate that ExM enables identifying cell types rare in a population, such as cells in mitosis and cytokinesis. Three-dimensional reconstruction of an entire volume of these cells provided details on the morphology of the mitotic spindle and the cleavage furrow. Finally, we show that established antibody markers of major cytoskeletal structures function well in ExM, which together with the ability to visualize proteins tagged with small epitope tags will facilitate studies of the kinetoplastid cytoskeleton.

1. Introduction

Kinetoplastida are a group of protists, comprising both free-living and parasitic organisms. Of these, the most notorious are *Trypanosoma brucei* (the causative agent of African sleeping sickness in humans and nagana in cattle), *T. cruzi* (causing Chagas disease in Americas) and numerous species of *Leishmania* genus (causing cutaneous, mucocutaneous and visceral leishmaniasis on several continents). These important parasites are transmitted between mammalian hosts by insect vectors. Progression of infection in both the host and the vector is dependent on the ability of the parasites to colonize, in a defined sequence, various tissues. To achieve so, transitions between various proliferative life cycle forms occur via differentiation events associated with dramatic changes to cell shape, size and arrangement of organelles [1].

Despite the considerable morphological diversity, kinetoplastid cells share a common design principle with their morphology being determined by the microtubule-based cytoskeleton; the microtubules form the subpellicular corset, an array of

parallel evenly spaced microtubules, which subtend the entire cytoplasmic membrane [2]. Another prominent feature is the presence of the flagellum, the principal motility organelle, which contains the evolutionarily conserved microtubule-based axoneme, and the kinetoplastid-specific paraflagellar rod [2]. The flagellum specifies, via association with its base, the position of single-copy organelles, such as the kinetoplast (i. e. mitochondrial DNA) and the flagellar pocket [3]. Moreover, in *T. brucei*, the attachment of the flagellum to the cell body via the structure called the flagellum attachment zone (FAZ) defines cell shape, polarity and the starting point of cytokinesis [4]. Replication of these cytoskeletal structures is coordinated and tightly linked to the cell cycle, and occurs with high fidelity [5]. Thus, kinetoplastid cells of a proliferative population show a remarkable uniformity of their cytoskeletal architecture.

Studies of the kinetoplastid cytoskeleton have been heavily reliant on electron microscopy (EM), mainly due to the spacing of various structural components, such as the corset microtubules, axonemal microtubule doublets and domains of the FAZ, being below the resolution limit of conventional light microscopy, which is about 180 nm in the lateral and 500 nm in the axial direction [6]. Indeed, EM provided a considerable understanding of the kinetoplastid cytoskeletal architecture (e.g. [5,7,8]). However, the EM approaches require specialized reagents, instrumentation, and are time demanding, making certain types of studies challenging. These include for example an ultrastructural investigation of cells that are rare in a population; yet these may be key for understanding life cycle transition processes. Another example is studies aiming to determine the localization of specific molecules in the entire cellular volume. Similar limitations also apply to major super-resolution optical microscopy techniques, such as STED and STORM [6].

Over recent years, another super-resolution method, termed expansion microscopy (ExM), was developed [9,10]. It is based on embedding a specimen into a swellable polymer and its subsequent isotropic expansion. These specimens, typically expanded 4–5 times in each direction, are thereafter imaged with a confocal microscope; this produces a corresponding increase in resolution and is comparatively rapid.

ExM has been extensively employed to study mammalian cells and tissues (e.g. [11–13]). By contrast, only a limited number of studies of parasitic protists have been conducted so far. Yet investigations of *Giardia intestinalis* [14] and *Plasmodium* [15], as well as the recent study of a mitochondrial genome segregation factor in *T. brucei* [16], demonstrated that due to small sizes of their cells ExM offers clear opportunities for analysing structural features of these important parasites. Moreover, due to a well-defined morphology of their cellular cytoskeleton protists enable assessing the ExM approach at cellular dimensions.

In this work, we set out to optimize and validate ExM for *Trypanosoma brucei* and *Leishmania major* cells, which possess a complex, highly defined and relatively well-characterized microtubule-based cytoskeleton, as described above. We show that data obtained by ExM recapitulate the previous EM observations with regard to the presence, positioning, orientation and shape of individual structures. However, caution should be observed when using ExM to determine distances, as individual structures may expand to a different extent. This was previously noticed in other experimental systems (e.g. [17,18]). Importantly, we observed that ExM enables resolving individual cytoskeletal components, such as the microtubules.

This, together with the quantitative aspect of the approach, facilitated a better understanding of less well-appreciated structures, such as the neck microtubule in *T. brucei*, or the pocket, cytoplasmic and multivesicular tubule-associated microtubules in *L. major*. We further observed in a subset of *L. major* cells short microtubules or plate-like structures associated with basal and pro-basal bodies. Moreover, ExM facilitated studies of rare cell types in a population, providing detailed information on the structure of the mitotic spindle and cleavage furrow in *L. major*.

Finally, we demonstrate that a number of commonly used antibody markers can be used to visualize the respective cytoskeletal structures by ExM as well as localize epitope-tagged proteins in the entire cellular volume. We envisage that, due to its robustness, flexibility and rapid image acquisition, ExM will become a valuable approach to study the biology of the kinetoplastid parasites.

2. Results

2.1. Optimizing expansion microscopy for kinetoplastid cells

To optimize and validate the ExM protocol for kinetoplastids, we used procyclic *T. brucei brucei* cells, which naturally occur in the tsetse fly midgut. They can, however, be readily cultured in a laboratory, and hence their morphology, cellular architecture and changes to these during the cell cycle have been extensively characterized [5,7].

We employed a variation of ExM termed ultrastructure ExM, which is based on fixation of cells with 4% formaldehyde and 4% acrylamide, followed by gelation with 19% sodium acrylate, 10% acrylamide and 0.1% N, N'-methylenebisacrylamide, denaturation with 200 mM sodium dodecyl sulfate at 95°C, and antibody staining [10]. Following a described protocol for handling free-swimming *Chlamydomonas* cells [10], we adhered procyclic *T. brucei* cells to a glass coverslip and further processed for ExM. To visualize expanded microtubule-based structures to validate the procedure, we tested several anti-tubulin antibodies: the polyclonal rabbit anti-alpha tubulin antibody (table 1 for specification), the mouse monoclonal anti-alpha tubulin antibody TAT1 [19], the mouse anti-beta tubulin antibody KMX-1 [20] and the mouse monoclonal anti-acetylated tubulin antibody C3B9 [19].

A three-dimensional volume reconstructed from a series of confocal z-planes of expanded cells revealed that the anti-tubulin signal of each of the antibodies outlined the entire microtubule corset (figure 1a; electronic supplementary material, figure S1). The corset retained its typical elongated shape, including being wider at the posterior cell end than at the anterior end, as demonstrated previously by light microscopy [25], as well as by EM [5]. To estimate the expansion factor, we turned the z-stacks into two-dimensional images by applying maximum intensity projection and measured the length of the corsets; these were 70–110 µm long. Corsets of formaldehyde-fixed non-expanded cells imaged by confocal microscopy (figure 1b) were 16–24 µm long, yielding the expansion factor of approximately 4.5. This is in agreement with the measured 4.7-fold physical expansion (4.58, 4.66 and 4.71-fold expansion in three experiments) of the gel in water prior to imaging.

Tilting three-dimensional reconstructed corsets revealed that they were significantly flattened on the side juxtaposed

Table 1. List of used antibodies. ExM—expansion microscopy; IF—immunofluorescence.

primary antibody	target	source	raised in	dilution for ExM	dilution for immunofluorescence
polyclonal anti-alpha tubulin	alpha tubulin	Genetex GTX 15246	rabbit	1 : 20	1 : 10
TAT1	alpha tubulin	Woods <i>et al.</i> [19]	mouse	1 : 10	1 : 100
KMX-1	beta tubulin	Birkett <i>et al.</i> [20]	mouse	1 : 10	1 : 100
C3B9	acetylated alpha tubulin	Woods <i>et al.</i> [19]	mouse	1 : 10	1 : 100
L3B2	FAZ1 constituent of FAZ	Kohl <i>et al.</i> [21]	mouse	1 : 10	1 : 40
anti-ClpGM6 (CUK1114)	ClpGM6 constituent of FAZ	Hayes <i>et al.</i> [3]	rabbit	1 : 200	1 : 200
L8C4	PFR2 constituent of PFR	Kohl <i>et al.</i> [21]	mouse	1 : 10	1 : 20
anti-HA tag	HA tag	Cell Signaling Technology 37245	rabbit	1 : 500	1 : 500
mAb25	axonemal protein TbSAXO	Pradel <i>et al.</i> [22]	mouse	1 : 25	1 : 20
anti-FTZC	flagellum transition zone component	Bringaud <i>et al.</i> [23]	rabbit	1 : 500	1 : 1000
did not produce any specific signal in ExM					
BBA4	BB and pro-BB	Woods <i>et al.</i> [19]	mouse	1 : 50	1 : 100
mAb62	flagella connector	Abeywickrema <i>et al.</i> [24]	mouse	1 : 25	1 : 500
secondary antibody	source	raised in	dilution for ExM	dilution for immunofluorescence	
alexa fluor 488 anti-mouse IgG (H + L)	Invitrogen A11001	goat	1 : 500	1 : 1000	
alexa fluor 488 anti-rabbit IgG (H + L)	Invitrogen A11008	goat	1 : 500	1 : 1000	
alexa fluor 555 anti-mouse IgG (H + L)	Invitrogen A21422	goat	1 : 500	1 : 1000	
alexa fluor 555 anti-rabbit IgG (H + L)	Invitrogen A21428	goat	1 : 500	1 : 1000	

to the surface of the gel (figure 1*a,c*). We assumed this flattening resulted from the adhesion of live cells to the glass surface at the beginning of the ExM procedure. Indeed, we observed similar flattening of non-expanded cells, which were attached to glass alive (figure 1*b*). Such a reduction in the cell height may be beneficial, as imaging thick specimens is subject to a significant signal loss and aberrations [26]. However, to obtain a more realistic visualization of the shape of the corset, we adapted the procedure for the preparation of specimens for scanning EM [3]. Live cells were first fixed in solution, settled onto a coverslip and thereafter processed for ExM. This indeed led to only a very limited area of a cell being flattened (figure 1*d*; electronic supplementary material, figure S1). To mitigate the signal loss we tried to match the refractive index of the gel to the one of the oil immersion by incubating it with a solution of 84% sucrose [27]. This indeed partially reduced the signal loss, but in accordance with previous observations [27] also led to a 10% reduction in the gel size with the final expansion factor of 4.3. Therefore, the approach was not universally employed in this study.

In contrast with non-expanded cells, in which the anti-tubulin antibodies stained the axonemal microtubules only

weakly (figure 1*b*; electronic supplementary material, figure S2, see also [19]), there was a strong signal associated with this structure in expanded specimens (figure 1*a,c,d*; electronic supplementary material, figure S1). Hence, the axoneme could be traced continuously from the point of its exit from the corset, running in an incomplete turn alongside the corset, and extending beyond its anterior end (figure 1*a,c,d*; electronic supplementary material, figure S1), consistent with previous observations [25]. A gap between the corset and the axoneme was always present. This space is occupied by the cellular and flagellar membranes and also contains the junction complex of the FAZ [28] (see below for antibody staining against the FAZ constituents).

Dividing cells were readily identifiable by the presence of two axonemes. The distal end of the new axoneme was found in the proximity of the old axoneme with a gap separating the two (figure 1*c,d*; electronic supplementary material, figure S1). It had been shown that this space is occupied by the membrane junction termed the flagella connector [29]. Due to the ability to rapidly screen cells in a population at a low magnification, it was straightforward to identify and image rarer cell types, such as cells in various stages of cytokinesis (figure 1*c,d*; electronic supplementary material,

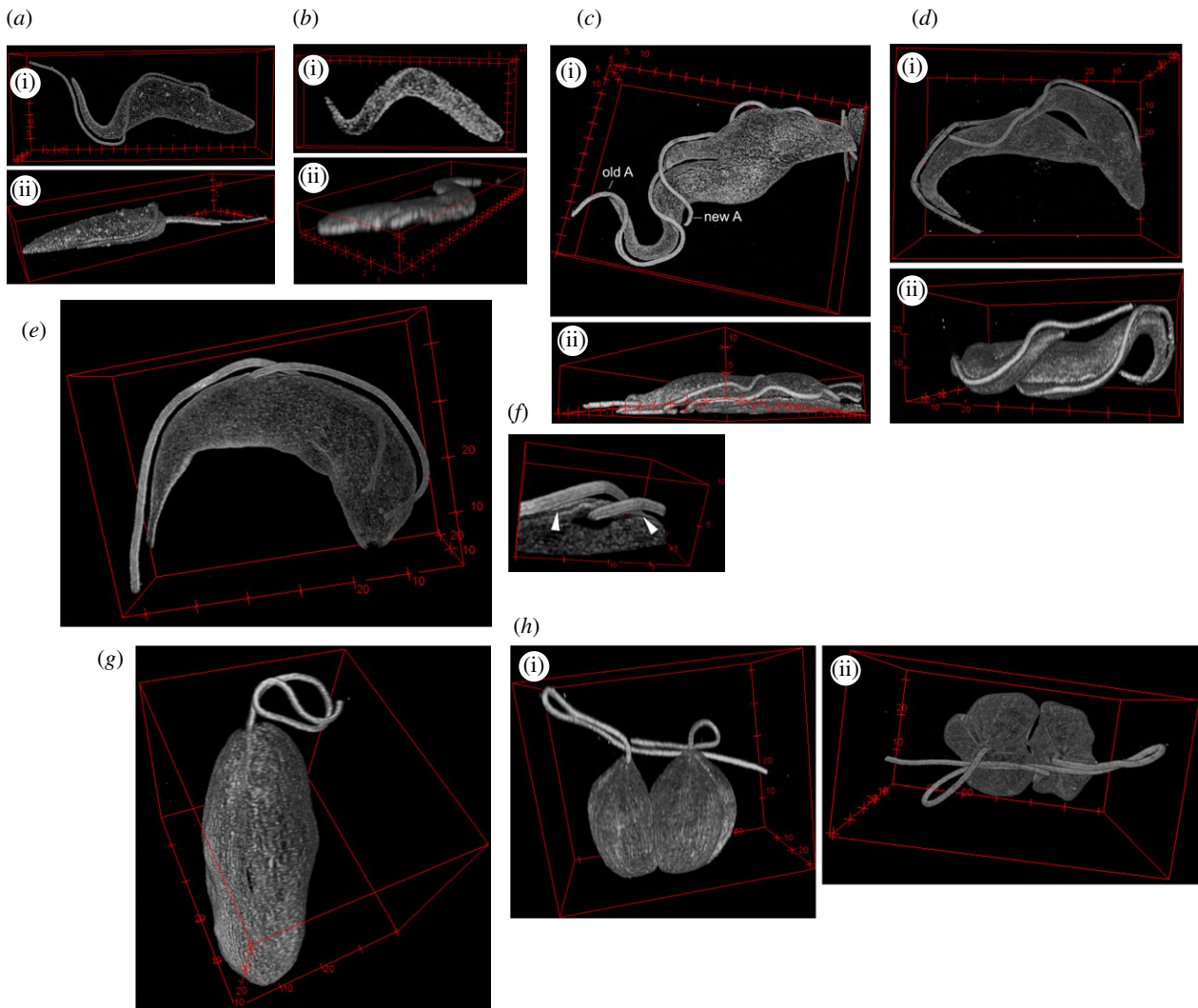


Figure 1. ExM visualizes three-dimensional morphology of the subpellicular corset and the axoneme. (a) Three-dimensional reconstruction of a confocal z-stack of a procyclic *T. brucei* cell fixed on a coverslip and stained with the rabbit polyclonal anti-tubulin antibody. (i) En face view; (ii) side view. Axes labels are in μm for all three-dimensional reconstructed images. (b) Three-dimensional reconstruction of a confocal z-stack of a non-expanded procyclic *T. brucei* cell fixed on a coverslip and stained with the C3B9 antibody. (i) en face view; (ii) side view. (c) Three-dimensional reconstruction of a confocal z-stack of a procyclic *T. brucei* cell in cytokinesis, which was fixed on a coverslip and stained with the C3B9 antibody. (i) En face view; (ii) side view. old A—old axoneme; new A—new axoneme. (d) Three-dimensional reconstruction of a confocal z-stack of an expanded procyclic *T. brucei* cell in cytokinesis, which was fixed in solution before being settled on a coverslip and stained with the C3B9 antibody. (i) En face view; (ii) side view. (e) En face view of three-dimensional reconstruction of an expanded bloodstream *T. brucei* cell stained with the C3B9 antibody. (f) Three-dimensional reconstruction of the area around the distal end of the new flagellum. Note the groove devoid of the microtubule signal, which houses the end of the new axoneme. In addition, lines underneath both axonemes devoid of the signal (arrowheads) correspond to the position of the FAZ filament. (g) En face view of three-dimensional reconstruction of an expanded *L. major* cell with a single flagellum stained with the C3B9 antibody. (h) Three-dimensional reconstruction of an expanded *L. major* cell with two flagella undergoing cytokinesis. The cell was stained with the TAT1 antibody. (i) Side view; (ii) view from anterior end.

figure S1B). In these cells, the cleavage furrow was clearly discernible and the non-equivalence of nascent daughter cells apparent, with the new flagellum daughter having a longer free flagellum overhang and a non-tapered anterior end (figure 1c,d; electronic supplementary material, figure S1B) [24].

Similarly to the procyclic cells, staining expanded bloodstream *T. brucei* cells with the anti-tubulin antibodies facilitated visualization of the shape of the corset and the axoneme (figure 1e). The increased resolution made discernible the area of missing anti-tubulin signal surrounding the distal end of the new axoneme (figure 1f). This corresponds to the groove, an indentation of the cell body membrane with an associated gap in the subpellicular corset originally observed by serial block-face scanning EM [30]; ExM enabled for the first time visualization of the groove by light

microscopy. In addition to the groove, a line devoid of the signal extended alongside each axoneme; this area was likely occupied by the FAZ filament (figure 1f).

As *L. major* cells are of significantly smaller dimensions than *T. brucei* cells, their expansion prior to imaging would be very beneficial. Staining with the anti-tubulin antibodies indeed facilitated a three-dimensional reconstruction of corsets and axonemes of expanded promastigote *L. major* cells. We observed slender cells with a single flagellum as well as shorter and rounder cells in cytokinesis (figure 1g,h), recapitulating the previously described changes to the cell shape associated with the cell cycle progression [31,32]. The expanded cells were between 30 and 60 μm long, which, compared to non-expanded cells (6.5–13 μm) (electronic supplementary material, figure S3), implicated the expansion

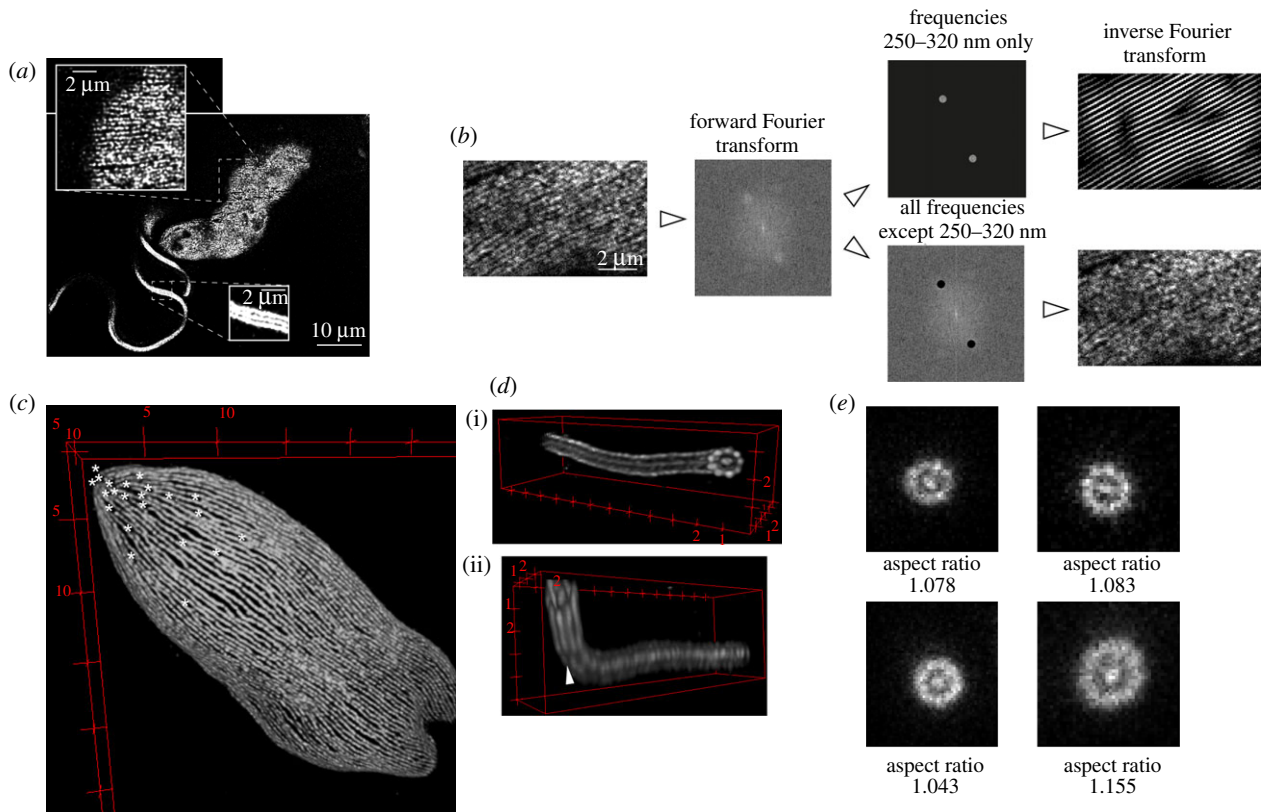


Figure 2. ExM resolves individual structural components. (a) A single confocal plane of an expanded procyclic *T. brucei* cell fixed on a coverslip and stained with the C3B9 antibody. The insets show the microtubule corset and the axoneme, respectively. (b) An example of an analysis of distances between microtubules in the subpellicular corset of procyclic *T. brucei*. Confocal z-planes encompassing corset microtubules in the vicinity of the coverslip and oriented approximately parallel to the image plane were projected to two-dimensional by the average intensity algorithm. The forward Fourier transform of the resulting image was performed. The frequency-domain image shows strongly represented frequencies with the periodicity of 250–320 nm. The inverse Fourier transform of these frequencies recapitulated the majority of the microtubule-associated signal (top), while the inverse Fourier transform of remaining frequencies did not (bottom). (c) Three-dimensional reconstruction of the posterior part of the subpellicular corset of a *L. major* cell (an identical cell to figure 1g). Ends of individual corset microtubules are indicated with asterisks. (d) Three-dimensional reconstruction of the distal part of the axoneme of a procyclic *T. brucei* cell. (i) View from the very end with nine doublets and central pair discernible. (ii) Tilted view showing the region in which the axoneme bends and is no longer perpendicular to the imaging plane. This is associated with a decreased resolution not enabling to discern each doublet (arrowhead). (e) Examples of axonemal regions of procyclic *T. brucei* cells analysed for how much they deviated from circularity by determining the aspect ratio of the major and minor axis of a fitted ellipse. Sum of five consecutive z-planes is shown. For remaining analysed regions see the electronic supplementary material, figure S5.

factor of approximately 4.6, similar to the one observed for procyclic *T. brucei* cells.

Three-dimensional reconstruction of cytoskeletons of cells in cytokinesis revealed that the cleavage furrow partitioned the cytoskeleton along the anterior–posterior axis of the cell body between the two flagella (figure 1h). The last point of attachment of two daughter cells was at their very posterior end (figure 1h), as was previously described by scanning EM [32] and at a lower magnification also by differential interference contrast microscopy [31].

2.2. Expansion microscopy resolves individual structural components

Inspecting confocal planes revealed that in many individual corset microtubules could be discerned (figure 2a). This was particularly the case when the microtubules were oriented parallel to the imaging plane and close to the surface of the gel, with the concomitantly high-signal intensity. To estimate the lateral spacing of the microtubules, we performed the forward Fourier transform of images of 10 such regions (for an example see figure 2b). The resulting frequency-domain images showed

strongly represented frequencies with periodicities within an interval with boundaries of 270 ± 30 nm (mean \pm s.d.) and 330 ± 50 nm, and with the mean value of 300 nm. These frequencies indeed accounted for the majority of observed microtubule-associated signal (figure 2b). The spacing of corset microtubules was previously determined by transmission EM as being 24 nm [7]. Taking into account the microtubule diameter of about 25 nm, the centre to centre distance of two adjacent microtubules in an unexpanded cell is about 50 nm. This implicates an expansion factor of 6.0, significantly higher than the expansion factor of the gel (4.7).

The antibodies KMX-1, TAT1 and C3B9 produced staining of a higher density and lower background than the rabbit anti-tubulin antibody. However, using none of these anti-tubulin antibodies, it was possible to reliably determine where individual microtubules terminated in corsets of *T. brucei* (e.g. figure 2a,b). This was, however, possible in *L. major*, mainly due to larger distances between corset microtubules in expanded cells (periodicities within an interval of 310 ± 20 nm to 470 ± 30 nm, $n = 11$ cytoskeletal regions; see also electronic supplementary material, figure S4). This, for example, enabled visualization of the high concentration of microtubule ends at the posterior end of the cell (figure 2c).

In individual confocal planes axonemal microtubule doublets were readily noticeable (figure 2*a*). In regions where the axoneme was oriented perpendicular to the imaging plane, it was possible to discern all nine doublets and the central pair, which was typically seen as a unit (figure 2*d*). The three-dimensional reconstruction revealed that in other regions not all the doublets were resolved (figure 2*d*), owing to the significantly worse axial than lateral resolution in light microscopy [6].

Based on transmission EM data, the axoneme is considered to be circular in its cross-section [33], enabling us to assess whether the expansion in ExM was isotropic. We analysed 27 axonemal regions of procyclic *T. brucei* specimens expanded either in water or in 84% sucrose, in which the axonemes were oriented perpendicular to the imaging plane. Fitting an ellipse to the axonemal cross-sections revealed that the aspect ratio between the major and minor axis was in all cases close to one (figure 2*e*; electronic supplementary material, figure S5; i.e. the expanded axonemes were nearly circular). There was no significant difference between specimens expanded in water (1.099 ± 0.037 , $n = 9$) and in sucrose (1.096 ± 0.044 , $n = 18$).

Furthermore, the diameter calculated from the circle area was $1.060 \pm 0.022 \mu\text{m}$ for nine specimens expanded in water, and $0.946 \pm 0.010 \mu\text{m}$ for 18 specimens expanded in sucrose. When divided by the diameter of the axoneme (220 nm according to [34]), it yielded the expansion factor of 4.8 in water and 4.3 in sucrose, well in accord with the measured expansion factors of gels (4.7 and 4.3, respectively).

2.3. Expansion microscopy facilitates studies of structures inside the corset

Intriguingly, ExM also facilitated visualization of tubulin-based structures located inside the corset. In both procyclic ($n = 38$ analysed cells) and bloodstream ($n = 14$) *T. brucei* cells, these were found in the basal body (BB) area around the proximal part of the flagellum. Their identity and organization became apparent when a three-dimensional volume of the area was reconstructed (figure 3*a,b*), as there was a very good agreement with the previously published model based on electron microscope tomography [7].

The strongly labelled BB could be distinguished at the base of the flagellum. The BB transited via a hollow transition zone into the axoneme, which was identifiable by the presence of the central pair. The axoneme exited the corset via a space visibly devoid of the microtubules. The pro-basal body (pBB) was located adjacent to each BB, and its orientation could be determined. Furthermore, a ribbon-like structure was spiralling alongside the proximal part of each axoneme. The structure started on the side of the BB facing the pBB and extended towards the corset, with which it merged. The position, shape and the fact, that it was stained by various anti-tubulin antibodies (electronic supplementary material, figure S6) were consistent with the structure being the microtubule quartet (mtQ), which subtends the flagellar pocket [7]. The mtQ is typically formed by four microtubules [5,7]. Although in ExM images, the mtQ signal was substantially wider than the signal of a corset microtubule (figure 3*a,b*), it was not possible to resolve individual mtQ microtubules. This is consistent with the mtQ microtubules in the BB area being more tightly spaced than the corset microtubules (e.g. fig. 3*b* in [35]).

Interestingly, in expanded cells, a single microtubule extending alongside the mtQ but terminating before the mtQ integrated into the corset was noticeable (figure 3*a,b*; electronic supplementary material, figure S6), which corresponded to the neck microtubule previously described by electron microscope tomography [7]. In expanded procyclic cells, this neck microtubule was observed in 54 of 56 BB areas (associated with the single flagellum of non-dividing cells, the old flagellum in dividing cells with two flagella, or the new flagellum in dividing cells, which extended significantly past the exit point). Similarly, the neck microtubule was present in 21 of 22 BB areas in bloodstream cells (for an example, see figure 3*b*).

EM previously described an even higher complexity of the microtubule-based structures inside the corset of *Leishmania* [8,36]. Our ExM data were well in accord with this. Moreover, the quantitative aspect of ExM revealed a significant variability in the presence of some of these structures in a population of promastigote *L. major* cells. Importantly, we also observed that it was straightforward to segment individual structures inside the corset, which has a potential towards their detailed analysis in the future (figure 3*c*).

We reconstructed volumes of seven cells with a single flagellum and 17 cells with two flagella. All 41 axonemes present in these cells were subtended by the BB with the associated pBB (figure 3*c,d*). Moreover, all the axonemes had the mtQ extending alongside their proximal part (figure 3*c,d*). Unlike in *T. brucei*, the mtQs did not intercalate the corset (figure 3*c,d*), confirming the EM observations [8]. Although the signal associated with the structure in ExM was wider than a single corset microtubule (figure 3*c,d*), individual mtQ microtubules could not be resolved. This is consistent with smaller distances between microtubules in the mtQ than in the corset (fig. 4*e* in [36]; and fig. 3*d* in [8]). In four of the seven cells with a single flagellum a microtubule-based structure extending in an arch from the pBB towards the axoneme was present (figure 3*c,e*); it probably corresponded to the nascent mtQ previously observed by EM in this cell type [8].

Additional structures included pocket microtubules, observed alongside 20 axonemes on the opposite side to the mtQ (figure 3*d*), and cytoplasmic microtubules, which were also associated with 20 axonemes (only partially overlapping with the set of axonemes with the pocket microtubules), but ran orthogonal to the mtQ (figure 3*c,d*). Finally, we observed short microtubules or small plate-like structures attached to 14 of the 41 BBs or associated pBBs (figure 3*d*). It is worth noting that in a minority of cases morphology or positioning of these additional structures deviated from those described by EM, highlighting the significant degree of variability of the microtubule-based structures in the BB area of *Leishmania*. This, together with the lack of other positional information, such as the flagellar pocket membrane, in the ExM specimens, made in these cases classification of the structures challenging.

Intriguingly, inside the corset of 20 of the 24 reconstructed cells, one ($n = 17$) or two ($n = 3$) long microtubules were present. These microtubules were less straight than microtubules of the corset and extended from its anterior end to the central part (figure 3*c,e*). Occasionally, an entire microtubule was located in the central part (figure 3*e*; electronic supplementary material, figure S7). These microtubules corresponded to the microtubules associated with the multivesicular tubule observed by EM in cell sections [36]. Interestingly, all four

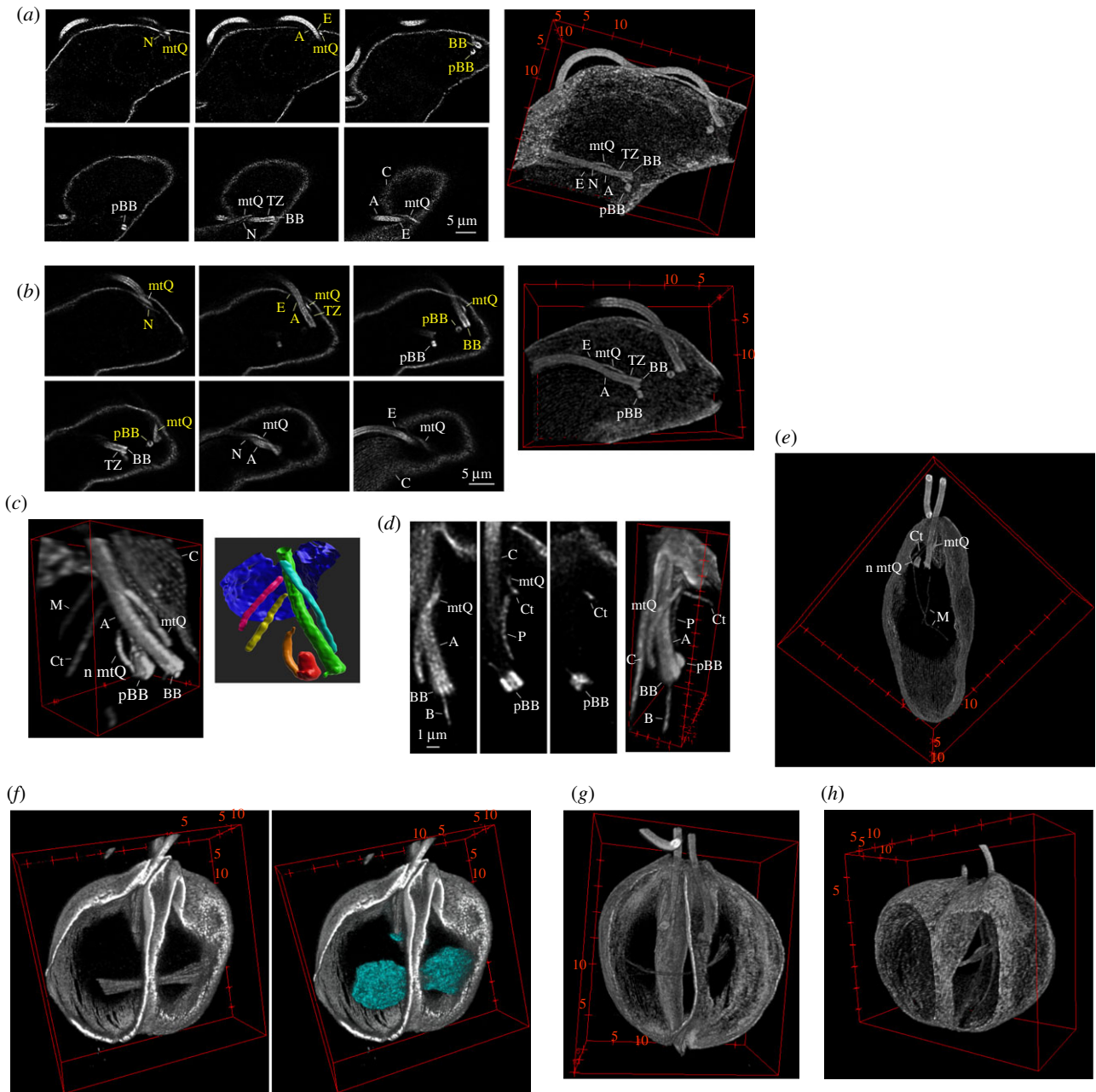


Figure 3. ExM facilitates studies of structures inside the corset. (a) Individual z-planes (left) and three-dimensional reconstruction (right) of the BB area of an expanded procyclic *T. brucei* cell (also shown in figure 1c) stained with C3B9. Yellow labels—structures associated with the new flagellum; white labels—structures associated with the old flagellum. A—axoneme; BB—basal body; pBB—pro-basal body; C—corset microtubules; mtQ—microtubule quartet; TZ—transition zone; E—exit of the flagellum from the corset; N—neck microtubule. Note that the mtQ signal is visibly broader than the signal of a single corset microtubule. Scale bar applies to all shown z-planes. (b) Individual z-planes (left) and three-dimensional reconstruction (right) of the BB area of an expanded bloodstream *T. brucei* cell (the cell shown in figure 1e) stained with C3B9. Yellow—structures associated with the new flagellum; white—structures associated with the old flagellum. A—axoneme; BB—basal body; pBB—pro-basal body; C—corset microtubules; mtQ—microtubule quartet; TZ—transition zone; E—exit of the flagellum from the corset; N—neck microtubule. Note that the mtQ signal is visibly broader than the signal of a single corset microtubule. Scale bar applies to all shown z-planes. (c) Three-dimensional reconstruction of the BB area of an expanded *L. major* cell with a single flagellum (the cell shown also in figure 1g). The cell was stained with C3B9. A—axoneme; BB—basal body; pBB—pro-basal body; C—corset microtubules; mtQ—microtubule quartet; n mtQ—nascent mtQ associated with the pBB; Ct—cytoplasmic microtubules; M—part of a microtubule associated with the multivesicular tubule. Right—segmentation of individual structures: BB and axoneme in green; pBB in red; microtubule quartet in cyan; nascent microtubule quartet in orange; cytoplasmic microtubules in yellow; part of a microtubule associated with the multivesicular tubule in magenta; and the very anterior part of the corset shown in dark blue. (d) Individual confocal z-planes (left) and three-dimensional reconstruction (right) of the BB area associated with one of two flagella in an expanded mitotic *L. major* cell, which was stained with C3B9 (see also figure 3g). A—axoneme; BB—basal body; pBB—pro-basal body; C—corset microtubules; mtQ—microtubule quartet; P—pocket microtubules; Ct—cytoplasmic microtubules; B—individual microtubules extending from the BB or pBB. Scale bar applies to all shown z-planes. (e) View inside the three-dimensional reconstructed expanded *L. major* cell (identical to the cell in figure 1g) revealed long microtubules (M) probably corresponding to the previously described microtubules associated with the multivesicular tubule. Note also the morphology of the cytoplasmic microtubule (Ct), and the nascent (n mtQ) and existing microtubule quartet (mtQ) in the BB area (shown in a higher magnification in figure 3c). (f–h) View inside the three-dimensional reconstructed corsets of expanded mitotic *L. major* cells. The mitotic spindle became thinner and elongated (from f–h), ultimately having flared microtubule ends at the spindle poles. The spindle was surrounded by DNA as revealed by Hoechst stain (cyan). Note also the cleavage furrow separating the cells into two daughters along their anterior–posterior axis and approximately perpendicular to the spindle.

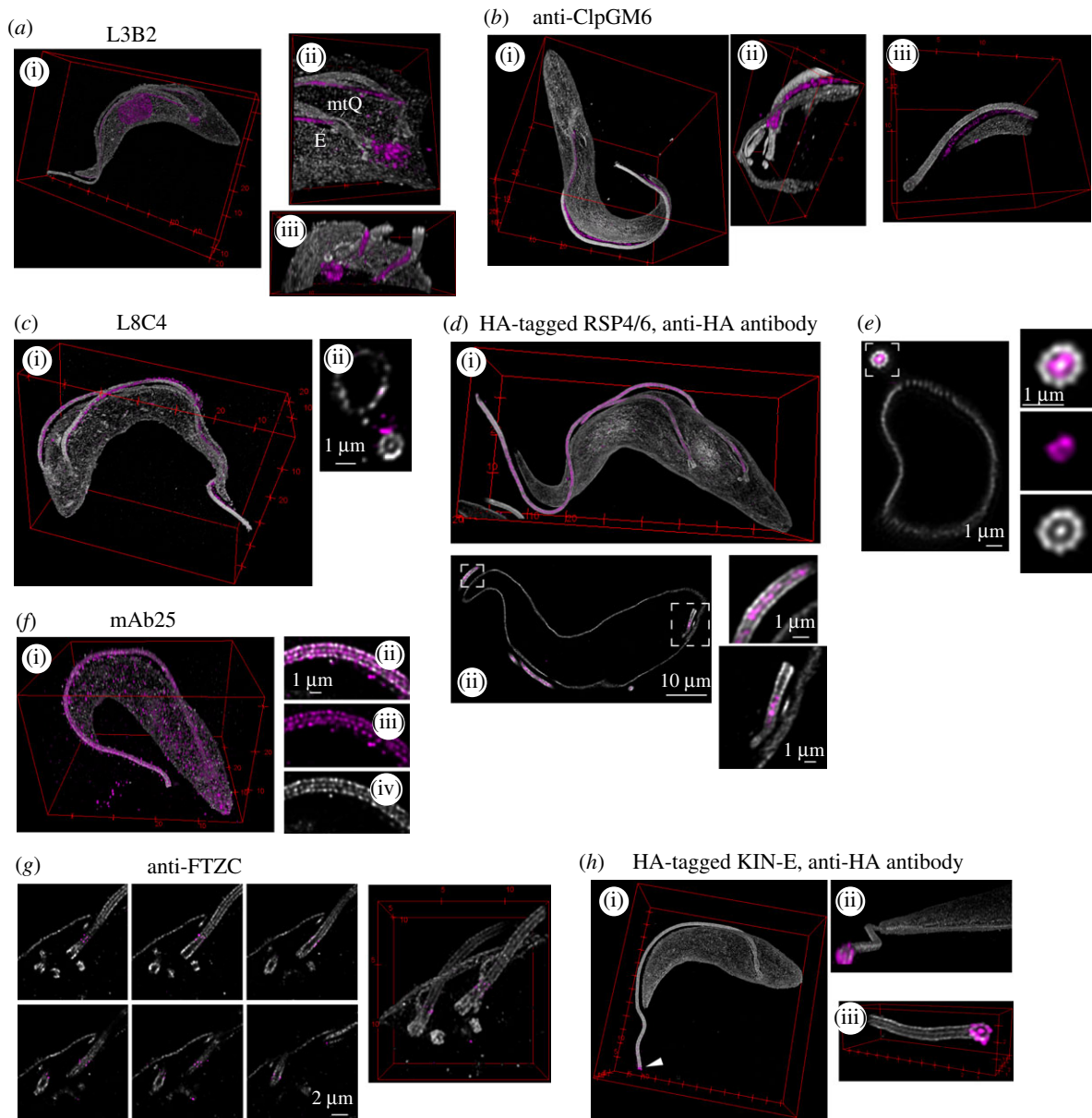


Figure 4. Localizing cytoskeletal proteins in respect to microtubule-based structures. Shown are expanded procyclic *T. brucei* cells, anti-tubulin signal shown in shades of grey, signal of antibodies to other cytoskeletal constituents in magenta. (a) Confocal imaging of a cell stained with L3B2 and the polyclonal anti-alpha tubulin antibody. (i) Three-dimensional reconstruction of the cellular volume; (ii) en face and (iii) from the anterior end view of the BB area without the bottom most part of the microtubule corset. E—exit of the flagellum from the corset; mtQ—microtubule quartet. Note the nuclear and kinetoplast signals produced by the antibody. (b) Confocal imaging of a cell stained with an anti-ClpGM6 antibody and C3B9 in a gel expanded in 84% sucrose. (i) Three-dimensional reconstruction of the cellular volume; (ii) a view of the three-dimensional reconstructed BB area without the bottom and top most corset microtubules; (iii) distal part of the axoneme with the anterior end of the corset of a cell different to the one shown on left, and imaged at a higher magnification. (c) Confocal imaging of a cell stained with L8C4 and the polyclonal anti-alpha tubulin antibody. (i) Three-dimensional reconstruction of the cellular volume; (ii) an orthogonal optical section through the anterior part of the cell. (d) Confocal imaging of a cell expressing HA-tagged RSP4/6 and stained with the anti-HA antibody and with C3B9. (i) Three-dimensional reconstruction of the cell. (ii) A single confocal plane of the cell. Insets show longitudinal optical sections through the axoneme and the proximal region of the flagellum. (e) A single confocal plane of a cell (different to the cell in (d)) expressing HA-tagged RSP4/6 and stained with the anti-HA antibody and with C3B9. The inset shows an optical cross-section through the axoneme—(top to bottom) merge, anti-HA signal, anti-tubulin signal. The images were acquired using $8 \times$ line averaging. (f) Confocal imaging of a cell stained with mAb25 and the polyclonal anti-alpha tubulin antibody. (i) Three-dimensional reconstruction of the cellular volume; (ii, iii, iv) a single confocal plane of the axoneme—(top to bottom) merge, mAb25 signal, anti-tubulin signal. (g) Confocal imaging of the BB area without the bottom and top most corset microtubules of a cells stained with FTZC and C3B9. Left—individual z-planes; Right—three-dimensional reconstruction. Scale bar applies to all shown z-planes. (h) Confocal imaging of a cell expressing $3 \times$ HA-tagged KIN-E and stained with the anti-HA antibody and with C3B9. (i) Three-dimensional reconstruction of the cellular volume. Arrowhead indicates the distal end of the flagellum with the anti-HA antibody signal. (ii) The view from the distal end of the flagellum of the cell on left. Note that both images come from a single confocal imaging and were obtained at an identical magnification. (iii) Confocal imaging of the distal end of a flagellum of a cell different to the one shown on left and acquired at a higher magnification. Note the unambiguous localization of KIN-E to the ends of all doublets and the central pair. Tubulin signal of the same axoneme is shown also in figure 2d.

cells in which no multivesicular tubule-associated microtubules were present were in mitosis. However, in other mitotic cells, these microtubules were observed.

In mitotic *Leishmania* cells, ExM visualized well the mitotic spindle, which was formed by a bundle of microtubules (figure 3f), as had been previously described by transmission

EM of serial sections [37]. In expanded cells, individual spindle microtubules were discernible, particularly at spindle poles. DNA staining demonstrated that the spindle was surrounded by the nuclear DNA, segregated by the spindle into two masses (figure 3*f*). Cells at later stages of mitosis possessed thin elongated spindles with flared microtubule ends localized at the poles (figure 3*g,h*). In observed mitotic cells, an ingression of the corset microtubules along the anterior–posterior cell axis was present (figure 3*f–h*). The cleavage plane was orthogonal to the axis connecting the BBs of the two flagella and to the long axis of the mitotic spindle (figure 3*g,h*).

2.4. Localizing cytoskeletal proteins in respect to microtubule-based structures

ExM has been frequently used to determine the position of various proteins in respect to microtubule-based structures (e.g. [14–16,38]).

Procytic *T. brucei* cells, due to their well-defined morphology, a considerable body of knowledge on protein localization acquired by EM, and availability of high-quality antibodies (see electronic supplementary material, figure S2) appear to be an excellent system to further validate the approach. First, we focused on FAZ and assessed whether ExM can differentiate proteins localizing to distinct domains of the structure. Staining expanded cells with the L3B2 antibody recognizing the FAZ1 protein [21,39] produced a linear signal starting below the point of the axoneme exiting the corset and intimately linked to the mtQ (figure 4*a*). It further extended along the corset following the axoneme and terminated at the anterior end of the corset (figure 4*a*). Importantly, the signal was positioned between microtubules of the corset and also extended below its surface (figure 4*a*). This is consistent with the localization of the FAZ1 protein to the FAZ filament domain in the cell body, as determined by immunogold EM [21,28]. In contrast with immunofluorescence microscopy, the antibody also stained the nucleus and the kinetoplast in ExM (figure 4*a*; electronic supplementary material, figure S2).

Another FAZ protein, ClpGM6, was previously shown by immunogold EM to constitute FAZ fibres in the FAZ flagellum domain linking the flagellar cytoskeleton to the membrane junction [40]. Staining expanded cells with the anti-ClpGM6 antibody [3] indeed produced a robust signal spanning the gap between the axoneme and the corset (figure 4*b*). The signal started around the point of the axoneme exiting the corset and terminated past its anterior end (figure 4*b*).

Next, we focused on individual structures of the flagellar cytoskeleton. First, we applied to expanded cells the L8C4 antibody, which recognizes a constituent of the paraflagellar rod [21], a kinetoplastid-specific structure extending alongside the axoneme. In ExM, the L8C4 signal was indeed juxtaposed to the axoneme (figure 4*c*). Despite its significant granularity, it was possible to determine that the signal started distal to the point of the axoneme exiting the corset and diminished towards the distal end of the axoneme, which is consistent with immunofluorescence observations (electronic supplementary material, figure S2; see also [21]).

As an example of a protein found inside the axoneme, we studied RSP4/6, an evolutionary conserved member of the

radial spokes connecting the microtubule doublets to the central pair [34]. As no antibodies against the trypanosome RSP4/6 are available, we tagged the protein at its endogenous locus with a 3 × HA tag and stained the resulting cells after expansion with an anti-HA antibody. In both, optical cross-sections and longitudinal sections, it was apparent that the anti-HA signal was confined within the space defined by the outer doublets (figure 4*d,e*). Moreover, in the orthogonal sections, it was noticeable that the central part was devoid of the signal; this corresponded to the space occupied by the central pair microtubules (figure 4*e*). ExM also revealed that the signal started just distal to the transition zone concomitant with the central pair microtubules (figure 4*d*).

Next, we studied localization of the protein *TbSAXO*. This microtubule-associated protein had previously been demonstrated to localize to the axoneme by immunogold EM [41] and has been used as an axonemal marker in *T. brucei*. Expanded cells stained with the mAb25 antibody [22] recognizing *TbSAXO* revealed a clear co-localization of the protein with tubulin in the axoneme (figure 4*f*). A further interpretation of the mAb25 staining, such as the point at which the signal started along the axoneme, was precluded by the relatively strong speckled background staining in and around the cell.

Finally, we assessed the level of positional information achievable by ExM for proteins localizing to discrete regions along the flagellar cytoskeleton. First, we stained expanded cells with an antibody against FTZC, the first described marker of the transition zone in trypanosomes [23]. ExM revealed that individual puncta of the signal surrounded microtubules of the transition zone (figure 4*g*). Next, we generated a procytic cell line expressing 3 × HA-tagged KIN-E, the protein localizing along with the flagellum and significantly enriched at the flagellum distal end [42]. In expanded cells, an anti-HA antibody indeed produced a robust staining at the very end of the axoneme (figure 4*h*). Intriguingly, the resolution provided by ExM allowed to unambiguously localize KIN-E to the distal end of each axonemal doublet as well as to the central pair (figure 4*h*).

3. Discussion

In this work, we set out to assess the ExM approach for studying cytoskeletal structures using unicellular kinetoplastid parasites. Morphology of their cytoskeleton, particularly in the case of procytic and bloodstream *T. brucei* cells, had been extensively characterized by various EM approaches, with a remarkably little variation between cells in a population. We observed that ExM is capable of faithfully reproducing information on the presence, positioning, and morphology of structures and structural components. A prime example being the mtQ which in three-dimensional reconstructed cellular volumes obtained by ExM had an identical position, helical pattern and handedness as those previously determined by EM tomography [7]. Other notable examples include the groove of the bloodstream cells, so far observed only by serial block-face scanning EM [30], and differential localization of proteins to individual domains of the FAZ, previously determined by immunogold EM [21,40]. Hence, ExM can serve as a substitute of these EM approaches, which require highly specialized instrumentation, when the lateral resolution of about 50 nm suffices.

Our analysis of the axoneme shape showed that the expansion was isotropic, which is consistent with published observations of tissues, cells, organelles and structures [10,12,43]. Our data, however, also indicated that the degree of expansion was not identical for the studied cytoskeletal structures; while the axoneme expanded 4.8-fold, similar to the 4.7 expansion factor of the gel, the distance between the corset microtubules increased 6.0-fold. Leaving aside the potential caveats associated with estimating dimensions from EM data [44], which were used to calculate these expansion factors, similar and higher discrepancies in expansion factors of individual organelles were recently observed in various experimental systems and using a variety of ExM protocols [17,18,45,46]. Hence, it seems likely that based on their composition individual organelles and structures undergo differential expansion, precluding a straightforward interpretation of measured distances between entities of expanded specimens.

Despite these limitations, there are characteristics which make ExM well suited to complement EM approaches for answering specific questions.

- (i) Foremost, ExM is based on immunofluorescence staining and standard confocal microscopy, with image acquisition and subsequent three-dimensional reconstruction being comparatively rapid. Hence, it is straightforward to obtain three-dimensional volumes of tens of cells, as presented here, with even hundreds of cells manageable. This would be challenging with EM approaches and facilitates quantitative super-resolution studies of cytoskeletal structures. Examples presented in this study include the observation of the neck microtubule being an integral part of the BB area in procyclic and bloodstream *T. brucei* cells, and that the mtQ is found alongside every axoneme in promastigote *L. major* cells, while pocket microtubules, cytosolic microtubules and multivesicular tubule-associated microtubules are common, but not universally present.
- (ii) The real strength of ExM lies in the method offering the possibility of rapidly inspecting a population of cells and at the same time the ability to image an entire volume of a cell of interest at a relatively high resolution. This unique combination makes possible studies of rare cell types, such as cells in transient phases of the cell cycle, for example in cytokinesis (figure 1*c,d*, and *h*). In these cells, ExM visualized how the corset was partitioned by the cleavage furrow. In *L. major*, ExM also provided information on the morphology of the mitotic spindle, including observations of ends of individual microtubules at the spindle poles (figure 3*f-h*). In addition, ExM has an obvious potential to provide novel information on events leading to duplication of structures in the BB area and their re-organizations following initiation of the new flagellum construction (for example see figures 3*c* and 4*b*). Finally, we envisage that ExM will be in a similar way highly useful to study morphology and cellular architecture of various transient life cycle forms and the processes of cell differentiation.
- (iii) Protein localization by immunogold EM is challenging as antibodies frequently do not reach or recognize their epitopes in resin-embedded sections. By contrast, it has been observed that antibody markers established for the standard immunofluorescence staining generally also stain expanded specimens [11]. Our data are in line with this (table 1). Intriguingly, we observed that in expanded cells the anti-tubulin antibodies stained the axonemal

microtubules well, while they have been known to produce only a weak signal in non-expanded cells (figure 1*a-c*; electronic supplementary material, figure S2; see also [19]). This probably reflects an increased accessibility of their epitopes in the axoneme due its expansion. Such a positive effect of de-crowding due to ExM was previously described in other systems [12,47]. On the other hand, we observed that two tested antibodies, BBA4 staining the BBs and pBBs in *T. brucei* [19] and mAb62 staining the flagella connector [24] (see also electronic supplementary material, figure S2), did not produce any specific signal in ExM (electronic supplementary material, figure S8). This may stem from a degradation of respective epitopes during the SDS-based denaturation step of ExM, not present in a standard immunofluorescence protocol. An ExM approach based on a different homogenization step could be considered [48].

The applicability of ExM to localize proteins in these kinetoplastid species is further augmented by the available repertoire of reverse genetics approaches. We used the rapid PCR-only approach to generate cell lines expressing proteins of interest tagged at their endogenous loci with a small epitope tag [49]. The resolution of ExM images was sufficient to unambiguously localize the radial spoke protein RSP4/6 to the space between the axonemal microtubule doublets and the central pair, and the kinesin KIN-E to the tips of individual doublets as well as the central pair. Hence, this approach opens up the possibility of localizing in the cellular volume and at a relatively high resolution, many proteins encoded in genomes of these parasites.

In conclusion, ExM is a powerful approach for studying cytoskeletal structures in *T. brucei*, *L. major* and probably other kinetoplastid species. It is a simple, yet robust super-resolution method, which does not require highly specialized reagents or instrumentation. ExM data recapitulate well observations by various EM approaches. Moreover, ExM is capable of complementing them due to its ability to provide a highly quantitative information.

4. Material and methods

4.1. Cell growth and preparation of transgenic cell lines

Trypanosoma brucei brucei procyclic SmOxP927 cells [50] were cultured at 28°C in SDM-79 medium (Life Technologies) supplemented with 10% fetal bovine serum (Gibco, 10270106) [51]. Transgenic cell lines with flagellar proteins KIN-E (Tb927.5.2410 [42]) and RSP4/6 (Tb927.11.4480 [52]) tagged with a 3 × HA tag were generated using the pPOT tagging approach [49]. Bloodstream *Trypanosoma brucei brucei* cells of the 427 cell line and promastigote *Leishmania major* cells were provided by the laboratory of Martin Zoltner, Charles University, Prague, Czech Republic.

4.2. Expansion microscopy

4.2.1. Fixation of cells

For fixation on coverslips, 2×10^6 cells per specimen were used, and for fixation in solution 1×10^6 cells per specimen were used. The cells were pelleted by centrifugation for 5 min at

800 g, followed by two washes with PBS, or with PBS supplemented with 3.3 mM glucose (Penta, G01102) in the case of bloodstream *T. brucei* cells.

For fixation on coverslips, the cells were re-suspended in 50 μ l of PBS and transferred onto a coverslip (High Precision \varnothing 12 mm No. 1.5H, Marienfeld) placed in a 24-well plate (Jet Biofil, TCP011024), to facilitate subsequent steps. Following a 5 min incubation, the cells were washed with PBS and fixed with 500 μ l of a freshly prepared fixation solution containing 4% formaldehyde (Sigma, F8775) and 4% acrylamide (Sigma, A8887) in PBS. For fixation in solution, the cells were directly re-suspended in the fixation solution and transferred to a poly-L-lysine (Sigma, P4707) coated coverslip in a 24-well plate. In both cases, the cells were fixed overnight at room temperature, followed by a PBS wash.

4.2.2. Gelation

Gelation was performed on a strip of Parafilm in a wet chamber, which was initially placed on ice. The monomer solution containing 19% sodium acrylate (Sigma, 408220), 10% acrylamide and 0.1% N, N'-methylenebisacrylamide (Sigma, M7256) in PBS was aliquoted and stored at -20°C for up to a month. Immediately prior to gelation N, N, N', N'-tetramethylethylenediamine (Sigma, T9281) and ammonium persulfate (Thermo Scientific, 17874) were added to the monomer solution to the final concentration of 0.5% each, and 50 μ l of the mixture were quickly transferred onto Parafilm in the wet chamber. Coverslips with the cells facing down were placed on the drop of the monomer solution and incubated for 5 min. The wet chamber was subsequently transferred to 37°C and incubated for 30 min to allow for a proper gel polymerization.

4.2.3. Denaturation and expansion of the gel

The gelation chamber was brought to room temperature and several drops of ultrapure water were added to the coverslips to help the gel detach from Parafilm. Thereafter, the specimens were transferred to a well of a 12-well plate (Jet Biofil, TCP011012) containing 1 ml of the denaturation buffer consisting of 50 mM tris(hydroxymethyl)aminomethane-hydrochloride (Serva, 3719202), 200 mM sodium chloride (Lach-Ner, 30093-AP0), 200 mM sodium dodecyl sulfate (Roth, 1057) and pH 9.0. At this point, gels started to expand, which facilitated their separation from the coverslips. Gels together with the remaining denaturation buffer were transferred to a 1.5 ml microcentrifuge tube, which contained 0.5 ml of the denaturation buffer, and denaturation was performed for 1 to 2 h at 95°C . The denatured gels were transferred to \varnothing 10 cm Petri dishes and expanded by three 20 min incubations with 15 ml of ultrapure water.

4.2.4. Antibody staining of expanded specimens

Water was removed and an approximately 10×10 mm piece of the gel was cut per each antibody staining. Staining was performed in a 6-well plate (Jet Biofil, TCP011006), in the dark while gently rocking. Both primary and secondary antibodies were diluted in 500 μ l of the ExM blocking buffer consisting of 2% bovine serum albumin (Roth, 8076) in PBS. In general, we observed that both primary and secondary antibodies produced good results when used more concentrated compared to standard immunofluorescence experiments. For antibody

concentrations see table 1. The gels were first incubated overnight at room temperature with 500 μ l of diluted primary antibodies. Thereafter, they were washed by 3×20 min incubations with 3.5 ml of ultrapure water, followed by an overnight incubation with 500 μ l of secondary antibodies. Subsequently, the gels were washed 3×20 min with 3.5 ml of ultrapure water and selected specimens were also incubated for 30 min at room temperature with $10 \mu\text{g ml}^{-1}$ 4',6-diamidino-2-phenylindole (DAPI) (Sigma, D9542) or $10 \mu\text{g ml}^{-1}$ Hoechst 33342 (Thermo Scientific, 62249) in PBS while rocking. Finally, the gels were washed 5×15 min with 4 ml of ultrapure water. For co-staining experiments, specimens were simultaneously incubated with two primary or two secondary antibodies.

4.2.5. Imaging

Water was carefully aspirated, a stained piece of the gel was transferred to a centre of a glass-bottom dish (Cellvis, D35-20-1.5-N) coated with poly-L-lysine, and a small drop of ultrapure water was put on it to prevent drying. To facilitate imaging, it was important to keep track of the orientation of the gel during the procedure, such that the side of the gel with cells close to its surface was ultimately facing the glass-bottom dish. Specimens were imaged using a Leica TCS SP8 confocal microscope with an HC PL apochromatic 63x/NA 1.40 oil immersion objective. Excitation was performed with a 405 nm diode laser (50 mW) in the case of DAPI and Hoechst 33342, a 488 nm solid-state laser (20 mW) in the case of Alexa Fluor 488, and a 552 nm solid-state laser (20 mW) in the case of Alexa Fluor 555. Fluorescence was detected using hybrid detectors (HyD). Z-stacks were acquired with the step size of 100 nm. The pixel size was between 52 and 97 nm, and in the case of high magnification images between 18 and 36 nm. The pixel dwell time was 400 ns. The size of the pinhole was adjusted based on the signal strength, but was typically around 0.4 Airy unit to improve resolution. No averaging was used for z-stacks. In the case of a significant lateral drift, a piece of a gel was embedded in the two-component silicone-glue Twinsil (Picodent, 13001000). Expanded gels could be stored in Twinsil for several days before imaging.

4.3. Standard immunofluorescence staining

Procyclic *T. brucei* and promastigote *L. major* cells were washed and re-suspended in PBS to 1×10^7 cells ml^{-1} . 50 μm of *T. brucei* cells were transferred onto a cleaned \varnothing 12 mm coverslip, followed by a 4 min incubation. After removal of an excessive liquid, the cells were fixed for 5 min with 4% formaldehyde in PBS, washed 3×5 min with PBS and permeabilized for 10 min with 50 μm of 0.1% Triton X-100 (Roth, R30512) in PBS. 50 μm of *L. major* cells were transferred onto cleaned microscopic slides (Menzel Gläser, 630-1985), incubated for 4 min and an excessive liquid removed. The slides were transferred to an ice-cold methanol, incubated for 20 min at -20°C and rehydrated for 30 min in PBS. Both *T. brucei* and *L. major* specimens were subsequently washed for 3×5 min with PBS and incubated for 1 h with the IF blocking buffer consisting of 1% bovine serum albumin in PBS. Following another 3×5 min wash with PBS they were incubated for 1 h with primary antibodies diluted in the IF blocking buffer. Then, the specimens were washed for 3×5 min with PBS, incubated for 1 h with secondary antibodies diluted in the IF blocking buffer, washed,

mounted into a mounting medium containing 90% glycerol with 1,4-diazabicyclo[2.2.2]octane and 100 ng ml⁻¹ of DAPI, and stored at 4°C overnight. The specimens were subsequently imaged using a Zeiss Axioplan 2 microscope with a Zeiss 100x (NA 1.4) Plan Apochromat oil immersion objective and an Andor Zyla 4.2 camera controlled by Micromanager software [53].

4.4. Image analysis

Confocal z-stacks and individual images of non-expanded cells were processed and analysed in Fiji [54]. Three-dimensional reconstructions were performed in the 3D viewer plugin. To estimate the lateral spacing of microtubules areas of corsets with microtubules oriented parallel to the image plane were selected. Consecutive confocal z-planes encompassing a complete signal of these microtubules were projected to two-dimensional using the Average intensity algorithm (Image/Stacks/Z Project). Subsequently, the FFT command (Process/FFT/FFT) was used to compute the forward Fourier transform and display the resulting frequency-domain image. Using the oval selection tool areas of the frequency-domain image corresponding to the most strongly represented frequencies were selected and marked for the inverse Fourier transform by filling them with white colour. Subsequently, the inverse Fourier transform command (Process/FFT/Inverse FFT) was used to compute the inverse Fourier transform of these frequencies. To compute the inverse Fourier transform of the remaining frequencies, the areas corresponding to the most strongly represented frequencies were suppressed by filling them with black colour.

Selected z-stacks were deconvolved with Huygens Professional v. 19.10 (Scientific Volume Imaging, The Netherlands, <http://svi.nl>), using the CMLE algorithm. To segment selected cells their confocal z-stacks were reconstructed into a three-dimensional image using Imaris software 9.7.2 (Bitplane) and segmented by applying background subtraction (local contrast) threshold.

4.4.1. Assessing isotropy of expansion and extent of axonemal expansion

Isotropy of expansion was assessed on raw images (without deconvolution) based on the circular shape of the axonemal cross-section. First, axonemal regions perpendicular to the image plane were selected to avoid regions of elongated cross-sections due to the axoneme being tilted. The perpendicularity check was done in Fiji [54]. The default threshold method was applied to manually selected series of z-planes with a single axoneme present to create an axoneme binary mask. The close operation was performed on the binary

mask and the analyse particle tool was used to find the position of the mask centroid. For every five consecutive planes, the positions of the first and the fifth centroid were compared; if their *xy* coordinates were close to each other, they were further analysed. The threshold for the *xy* centroid distance was chosen as 4 × z-step size/tan(85 degrees), which corresponded to a 5 degree tilt. Twenty-seven selected axonemal stacks of five z-planes were corrected for the drift (StackReg plugin based on [55], Rigid Body transformation), summed (sum slices), and the default threshold method was used to create a binary mask. The circularity of the mask was assessed using the analyse particle tool by fitting an ellipse to the mask and extracting the aspect ratio of its major to minor axis. The aspect ratio of one indicates a circular object.

The analyse particle tool provided also the area of the ellipse. A diameter of a circle with an equivalent area was calculated. The diameter was corrected for blur due to light diffraction, estimated to be 200 nm (the value was obtained by distilling a point spread function in Huygens software from images of 100 nm beads acquired under conditions identical to z-stacks of cells). The corrected diameter divided by the typical diameter of the axoneme (220 nm according to [34]) yielded the expansion factor.

Data accessibility. This article has no additional data.

Authors' contributions. P.G.: involved in methods development, data acquisition, data analysis and writing manuscript. M.P.: involved in methods development, sample preparation and writing manuscript. H.V.: involved in methods development, sample preparation and writing manuscript. M.O.: involved in data analysis and writing manuscript. M.S.C.: involved in methods development and writing manuscript. V.V.: involved in experimental design, data analysis and writing manuscript.

Competing interests. We declare we have no competing interests.

Funding. Work in the Laboratory of cell motility was supported by the Czech Science Foundation (GA CR) project no. 20-23165J and by an Installation Grant from the European Molecular Biology Organization. V.V. is a holder of the J. E. Purkyne Fellowship of the Czech Academy of Sciences. The study was also supported by the Charles University project GA UK no. 972120 to P.G. We further acknowledge the Light Microscopy Core Facility, IMG CAS, Prague, Czech Republic, supported by MEYS (LM2018129, CZ.02.1.01/0.0/0.0/18_046/0016045) and RVO: 68378050-KAV-NPUI, for their assistance with the confocal imaging presented in this study, and Imaging Methods Core Facility at BIOCEV, institution supported by the MEYS CR (Large RI Project LM2018129 Czech-BioImaging) and ERDF (project no. CZ.02.1.01/0.0/0.0/18_046/0016045) for their support with data processing.

Acknowledgement. We are grateful to Farnaz Zahedifard and Martin Zoltnner for providing bloodstream *Trypanosoma brucei brucei* cells and promastigote *Leishmania major* cells. We thank Ludek Stepanek for assistance with image analysis and Keith Gull for providing antibodies and for critical comments on the manuscript. We further thank Derrick Robinson and Frederic Bringaud for providing antibodies.

References

1. Matthews KR. 2005 The developmental cell biology of *Trypanosoma brucei*. *J. Cell Sci.* **118**, 283–290. (doi:10.1242/jcs.01649)
2. Gull K. 1999 The cytoskeleton of trypanosomatid parasites. *Annu. Rev. Microbiol.* **53**, 629–655. (doi:10.1146/annurev.micro.53.1.629)
3. Hayes P, Varga V, Olego-Fernandez S, Sunter J, Ginger ML, Gull K. 2014 Modulation of a cytoskeletal calpain-like protein induces major transitions in trypanosome morphology. *J. Cell Biol.* **206**, 377–384. (doi:10.1083/jcb.201312067)
4. Kohl L, Robinson D, Bastin P. 2003 Novel roles for the flagellum in cell morphogenesis and cytokinesis of trypanosomes. *EMBO J.* **22**, 5336–5346. (doi:10.1093/emboj/cdg518)
5. Sherwin T, Gull K. 1989 The cell division cycle of *Trypanosoma brucei brucei*: timing of event markers and cytoskeletal modulations. *Phil. Trans. R. Soc. Lond. B* **323**, 573–588. (doi:10.1098/rstb.1989.0037)

6. Tam J, Merino D. 2015 Stochastic optical reconstruction microscopy (STORM) in comparison with stimulated emission depletion (STED) and other imaging methods. *J. Neurochem.* **135**, 643–658. (doi:10.1111/jnc.13257)
7. Lacomble S, Vaughan S, Gadelha C, Morpew MK, Shaw MK, McIntosh JR, Gull K. 2009 Three-dimensional cellular architecture of the flagellar pocket and associated cytoskeleton in trypanosomes revealed by electron microscope tomography. *J. Cell Sci.* **122**, 1081–1090. (doi:10.1242/jcs.045740)
8. Wheeler RJ, Sunter JD, Gull K. 2016 Flagellar pocket restructuring through the *Leishmania* life cycle involves a discrete flagellum attachment zone. *J. Cell Sci.* **129**, 854–867.
9. Chen F, Tillberg PW, Boyden ES. 2015 Expansion microscopy. *Science* **347**, 543–548. (doi:10.1126/science.1260088)
10. Gambarotto D *et al.* 2019 Imaging cellular ultrastructures using expansion microscopy (U-ExM). *Nat. Methods* **16**, 71–74. (doi:10.1038/s41592-018-0238-1)
11. Ku T *et al.* 2016 Multiplexed and scalable super-resolution imaging of three-dimensional protein localization in size-adjustable tissues. *Nat. Biotechnol.* **34**, 973–981. (doi:10.1038/nbt.3641)
12. Tillberg PW *et al.* 2016 Protein-retention expansion microscopy of cells and tissues labeled using standard fluorescent proteins and antibodies. *Nat. Biotechnol.* **34**, 987–992. (doi:10.1038/nbt.3625)
13. Zhao Y *et al.* 2017 Nanoscale imaging of clinical specimens using pathology-optimized expansion microscopy. *Nat. Biotechnol.* **35**, 757–764. (doi:10.1038/nbt.3892)
14. Halpern AR, Alas GCM, Chozinski TJ, Paredes AR, Vaughan JC. 2017 Hybrid structured illumination expansion microscopy reveals microbial cytoskeleton organization. *ACS Nano* **11**, 12 677–12 686. (doi:10.1021/acsnano.7b07200)
15. Bertiaux E, Balestra AC, Bournonville L, Louvel V, Maco B, Soldati-Favre D, Brochet M, Guichard P, Hamel V. 2021 Expansion microscopy provides new insights into the cytoskeleton of malaria parasites including the conservation of a conoid. *PLoS Biol.* **19**, e3001020. (doi:10.1371/journal.pbio.3001020)
16. Amodio S, Kalichava A, Fradera-Sola A, Bertiaux-Lequoy E, Guichard P, Butter F, Ochsenreiter T. 2021 Characterization of the novel mitochondrial genome segregation factor TAP110 in *Trypanosoma brucei*. *J. Cell Sci.* **134**, jcs254300. (doi:10.1242/jcs.254300)
17. Büttner M, Lagerholm CB, Waithe D, Galiani S, Schliebs W, Erdmann R, Eggeling C, Reglinski K. 2020 Challenges of using expansion microscopy for super-resolved imaging of cellular organelles. *ChemBioChem* **22**, 686–693. (doi:10.1002/cbic.202000571)
18. Pernal SP *et al.* 2020 Nanoscale imaging using differential expansion microscopy. *Histochem. Cell Biol.* **153**, 469–480. (doi:10.1007/s00418-020-01869-7)
19. Woods A, Sherwin T, Sasse R, Macrae TH, Baines AJ, Gull K. 1989 Definition of individual components within the cytoskeleton of *Trypanosoma brucei* by a library of monoclonal antibodies. *J. Cell Sci.* **93**, 491–500. (doi:10.1242/jcs.93.3.491)
20. Birkett CR, Foster KE, Johnson L, Gull K. 1985 Use of monoclonal antibodies to analyse the expression of a multi-tubulin family. *FEBS Lett.* **187**, 211–218. (doi:10.1016/0014-5793(85)81244-8)
21. Kohl L, Sherwin T, Gull K. 1999 Assembly of the paraflagellar rod and the flagellum attachment zone complex during the *Trypanosoma brucei* cell cycle. *J. Eukaryot. Microbiol.* **46**, 105–109. (doi:10.1111/j.1550-7408.1999.tb04592.x)
22. Pradel LC, Bonhivers M, Landrein N, Robinson DR. 2006 NIMA-related kinase TbNRKC is involved in basal body separation in *Trypanosoma brucei*. *J. Cell Sci.* **119**, 1852–1863. (doi:10.1242/jcs.02900)
23. Bringaud F, Robinson DR, Barradeau S, Biteau N, Baltz D, Baltz T. 2000 Characterization and disruption of a new *Trypanosoma brucei* repetitive flagellum protein, using double-stranded RNA inhibition. *Mol. Biochem. Parasitol.* **111**, 283–297. (doi:10.1016/S0166-6851(00)00319-4)
24. Abeywickrema M *et al.* 2019 Non-equivalence in old- and new-flagellum daughter cells of a proliferative division in *Trypanosoma brucei*. *Mol. Microbiol.* **112**, 1024–1040. (doi:10.1111/mmi.14345)
25. Alizadehrad D, Krüger T, Engstler M, Stark H. 2015 Simulating the complex cell design of *Trypanosoma brucei* and its motility. *PLoS Comput. Biol.* **11**, e1003967. (doi:10.1371/journal.pcbi.1003967)
26. Hell S, Reiner G, Cremer C, Stelzer EHK. 1993 Aberrations in confocal fluorescence microscopy induced by mismatches in refractive index. *J. Microsc.* **169**, 391–405. (doi:10.1111/j.1365-2818.1993.tb03315.x)
27. Gao M, Maraschini R, Beutel O, Zehtabian A, Eickholt B, Honigsmann A, Ewers H. 2018 Expansion stimulated emission depletion microscopy (ExSTED). *ACS Nano* **12**, 4178–4185. (doi:10.1021/acsnano.8b00776)
28. Sunter JD, Gull K. 2016 The flagellum attachment zone: ‘the cellular ruler’ of trypanosome morphology. *Trends Parasitol.* **32**, 309–324. (doi:10.1016/j.pt.2015.12.010)
29. Moreira-Leite FF, Sherwin T, Kohl L, Gull K. 2001 A trypanosome structure involved in transmitting cytoplasmic information during cell division. *Science* **294**, 610–612. (doi:10.1126/science.1063775)
30. Hughes L, Towers K, Starborg T, Gull K, Vaughan S. 2013 A cell-body groove housing the new flagellum tip suggests an adaptation of cellular morphogenesis for parasitism in the bloodstream form of *Trypanosoma brucei*. *J. Cell Sci.* **126**, 5748–5757.
31. Ambit A, Woods KL, Cull B, Coombs GH, Mottram JC. 2011 Morphological events during the cell cycle of *Leishmania major*. *Eukaryot. Cell* **10**, 1429–1438. (doi:10.1128/EC.05118-11)
32. Wheeler RJ, Gluenz E, Gull K. 2011 The cell cycle of *Leishmania*: morphogenetic events and their implications for parasite biology: the cell cycle of *Leishmania*. *Mol. Microbiol.* **79**, 647–662. (doi:10.1111/j.1365-2958.2010.07479.x)
33. Gadelha C, Wickstead B, Mckean PG, Gull K. 2006 Basal body and flagellum mutants reveal a rotational constraint of the central pair microtubules in the axonemes of trypanosomes. *J. Cell Sci.* **119**, 2405–2413. (doi:10.1242/jcs.02969)
34. Pigino G, Bui KH, Maheshwari A, Lupetti P, Diener D, Ishikawa T. 2011 Cryoelectron tomography of radial spokes in cilia and flagella. *J. Cell Biol.* **195**, 673–687. (doi:10.1083/jcb.201106125)
35. Höög JL, Bouchet-Marquis C, McIntosh JR, Hoenger A, Gull K. 2012 Cryo-electron tomography and 3-D analysis of the intact flagellum in *Trypanosoma brucei*. *J. Struct. Biol.* **178**, 189–198. (doi:10.1016/j.jsb.2012.01.009)
36. Weise F, Stierhof YD, Kühn C, Wiese M, Overath P. 2000 Distribution of GPI-anchored proteins in the protozoan parasite *Leishmania*, based on an improved ultrastructural description using high-pressure frozen cells. *J. Cell Sci.* **113**(Pt 24), 4587–4603. (doi:10.1242/jcs.113.24.4587)
37. Ureña F. 1986 Three-dimensional reconstructions of the mitotic spindle and dense plaques in three species of *Leishmania*. *Z. Parasitenkd. Parasitol. Res.* **72**, 299–306. (doi:10.1007/BF00928739)
38. Le Guennec M *et al.* 2020 A helical inner scaffold provides a structural basis for centriole cohesion. *Sci. Adv.* **6**, eaaz4137. (doi:10.1126/sciadv.aaz4137)
39. Vaughan S, Kohl L, Ngai I, Wheeler RJ, Gull K. 2008 A repetitive protein essential for the flagellum attachment zone filament structure and function in *Trypanosoma brucei*. *Protist* **159**, 127–136. (doi:10.1016/j.protis.2007.08.005)
40. Müller N, Hemphill A, Imboden M, Duvallet G, Dwinger RH, Seebeck T. 1992 Identification and characterization of two repetitive non-variable antigens from African trypanosomes which are recognized early during infection. *Parasitology* **104**, 111–120. (doi:10.1017/S0031182000060856)
41. Dacheux D, Landrein N, Thonnus M, Gilbert G, Sahin A, Wodrich H, Robinson DR, Bonhivers M. 2012 A MAP6-related protein is present in protozoa and is involved in flagellum motility. *PLoS ONE* **7**, e31344. (doi:10.1371/journal.pone.0031344)
42. An T, Li Z. 2018 An orphan kinesin controls trypanosome morphology transitions by targeting FLAM3 to the flagellum. *PLoS Pathog.* **14**, e1007101. (doi:10.1371/journal.ppat.1007101)
43. Chen F *et al.* 2016 Nanoscale imaging of RNA with expansion microscopy. *Nat. Methods* **13**, 679–684. (doi:10.1038/nmeth.3899)
44. Shah FA, Johansson BR, Thomsen P, Palmquist A. 2015 Ultrastructural evaluation of shrinkage artefacts induced by fixatives and embedding resins on osteocyte processes and pericellular space dimensions: ultrastructural evaluation of shrinkage artefacts. *J. Biomed. Mater. Res. A* **103**, 1565–1576. (doi:10.1002/jbm.a.35287)
45. Kubalová I, Schmidt Černohorská M, Huranová M, Weisshart K, Houben A, Schubert V. 2020 Prospects and limitations of expansion microscopy in chromatin ultrastructure determination.

- Chromosome Res.* **28**, 355–368. (doi:10.1007/s10577-020-09637-y)
46. Pesce L, Cozzolino M, Lanzanò L, Diaspro A, Bianchini P. 2019 Measuring expansion from macro- to nanoscale using NPC as intrinsic reporter. *J. Biophotonics* **12**, e201900018. (doi:10.1002/jbio.201900018)
 47. Sarkar D *et al.* 2020 Expansion revealing: decrowding proteins to unmask invisible brain nanostructures. *bioRxiv* 2020, 08.29.273540.
 48. Chozinski TJ, Halpern AR, Okawa H, Kim HJ, Tremel GJ, Wong ROL, Vaughan JC. 2016 Expansion microscopy with conventional antibodies and fluorescent proteins. *Nat. Methods* **13**, 485–488. (doi:10.1038/nmeth.3833)
 49. Dean S, Sunter J, Wheeler RJ, Hodgkinson I, Gluenz E, Gull K. 2015 A toolkit enabling efficient, scalable and reproducible gene tagging in trypanosomatids. *Open Biol.* **5**, 140197. (doi:10.1098/rsob.140197)
 50. Poon SK, Peacock L, Gibson W, Gull K, Kelly S. 2012 A modular and optimized single marker system for generating *Trypanosoma brucei* cell lines expressing T7 RNA polymerase and the tetracycline repressor. *Open Biol.* **2**, 110037. (doi:10.1098/rsob.110037)
 51. Brun R, Schönenberger M. 1979 Cultivation and in vitro cloning or procyclic culture forms of *Trypanosoma brucei* in a semi-defined medium. Short communication. *Acta Trop.* **36**, 289–292.
 52. Aslett M *et al.* 2010 TriTrypDB: a functional genomic resource for the Trypanosomatidae. *Nucleic Acids Res.* **38**, D457–D462. (doi:10.1093/nar/gkp851)
 53. Edelstein A, Amodaj N, Hoover K, Vale R, Stuurman N. 2010 Computer control of microscopes using µManager. *Curr. Protoc. Mol. Biol.* **92**, 14.20.1–14.20.17. (doi:10.1002/0471142727.mb1420s92)
 54. Schindelin J *et al.* 2012 Fiji—an open source platform for biological image analysis. *Nat. Methods* **9**, 676–682. (doi:10.1038/nmeth.2019)
 55. Thevenaz P, Ruttimann UE, Unser M. 1998 A pyramid approach to subpixel registration based on intensity. *IEEE Trans. Image Process.* **7**, 27–41. (doi:10.1109/83.650848)